Journal of Materials Chemistry A

ROYAL SOCIETY OF CHEMISTRY

PAPER

View Article Online
View Journal | View Issue

Cite this: J. Mater. Chem. A, 2023, 11, 17079

Heteroatom P filling activates intrinsic S atomic sites of few-layered $ZnIn_2S_4$ *via* modulation of H adsorption kinetics for sacrificial agent-free photocatalytic hydrogen evolution from pure water and seawater†

Boon-Junn Ng,[a] Wei-Kean Chong,[a] Lutfi Kurnianditia Putri,[a] Xin Ying Kong,[b] Jingxiang Low,[ac] Hing Wah Lee,[d] Lling-Lling Tan,[a] Wei Sea Chang[e] and Siang-Piao Chai *[a]

Received 10th November 2022
Accepted 13th March 2023

DOI: 10.1039/d2ta08789h

rsc.li/materials-a

The rational engineering of photocatalytic active sites on an atomic scale with regulated H adsorption energy and accelerated reaction kinetics has been pivotal to realize photocatalytic H_2 evolution reactions (HERs) without sacrificial reagents. Although hydrogen evolution from pure water splitting is at the forefront of solar H_2 research, photocatalytic seawater splitting is more in line with the notion of sustainable development owing to the limited resources of freshwater. Herein, we report for the first time an H adsorption kinetics-oriented design of two-dimensional (2D) hexagonal $ZnIn_2S_4$ (ZIS) atomic layers *via* heteroatom P doping (ZIS-P) for the modulation of intrinsic S active sites to achieve sacrificial agent-free photocatalytic HERs using both pure water and seawater. Atomic insights from density functional theory (DFT) calculations reveal that non-metal P dopants with different valence electrons and electronegativity than substituted S3 atoms in ZIS give rise to the formation of a new hybridized level with a moderately filled state near the valence band maximum (VBM) and impart redistribution of electron density within the coordination, hence triggering the activation of neighboring S2 atoms. Thus, ZIS-P with tailored S2 atomic sites and fine-tuned electronic structure endows a diminishment in H adsorption–desorption barriers and enables energetically favorable HERs. In particular, the optimal ZIS-P sample demonstrated visible light-driven photocatalytic water splitting without any sacrificial reagents, resulting in H_2 evolution rates of 1.68 μmol h^{-1} (pure water) and 1.54 μmol h^{-1} (simulated seawater), respectively. This work presents an approach to engineer the inert active sites, thus alleviating the strength of H adsorption free energy and enhance the HER kinetics.

Introduction

The concept of sustainable and clean hydrogen (H_2) economy is one of the major goals in renewable energy revolution to combat the prevalent and ever-growing energy crisis and environmental problems. Understandably then, tapping into the Earth's two most abundant and readily accessible free resources, *i.e.*, the Sun and water, in solar-to-hydrogen conversion has attracted global attention due to its enormous potential to meet the escalating energy demands.[1] In particular, direct solar water splitting using particulate photocatalysts presents a cost-effective approach for H_2 production due to its simplicity.[2–4] The latest advancements demonstrated that photocatalytic H_2 evolution reactions (HERs) could be achieved from pure water without sacrificial reagents.[5,6] However, using scarce pure water as the H_2 feedstock prompts a debatable argument on the

[a]Multidisciplinary Platform of Advanced Engineering, Chemical Engineering Discipline, School of Engineering, Monash University Malaysia, Jalan Lagoon Selatan, 47500 Bandar Sunway, Selangor, Malaysia. E-mail: chai.siang.piao@monash.edu

[b]School of Chemistry, Chemical Engineering and Biotechnology, Nanyang Technological University, 21 Nanyang Link, 637371 Singapore

[c]Department of Applied Chemistry, University of Science and Technology of China (USTC), 96 Jinzhai Road, Hefei, Anhui 230026, P. R. China

[d]Advanced Materials & Semiconductor Technology, MIMOS Berhad, Technology Park Malaysia, Kuala Lumpur 57000, Malaysia

[e]Mechanical Engineering Discipline, School of Engineering, Monash University Malaysia, Jalan Lagoon Selatan, 47500 Bandar Sunway, Selangor, Malaysia

† Electronic supplementary information (ESI) available: Composition of artificial seawater, FESEM image, EDX mapping and AFM of pristine ZIS, EDX spectroscopy of P-doped samples, enlarged XRD spectra, XPS spectra, photocatalytic HER performance of ZIS and ZIS-P200 in pure water and seawater, ˙OH trapping PL spectra, stability analysis and backward reaction testing of ZIS-P200, PL and TRPL spectra of ZIS and ZIS-P200. See DOI: https://doi.org/10.1039/d2ta08789h

infamous "food *versus* fuel" dilemma since pure water (fresh water) is deemed to be one of the valuable commodities that is essential to human survival.[7] Thus, precious freshwater should be utilized rationally to assure long-term sustainability of water resources. In light of this, interest has also peaked in photocatalytic HERs from seawater ascribed to its sheer magnitude on the Earth (93% of the planet's water reserve is made up of seawater).[8–11] Therefore, the rational development of photocatalytic materials that feature excellent HER kinetics and low reaction barrier is imperative to govern efficient H_2 evolution in both pure water and seawater, further idealizing the practicability of grid-scale solar H_2 industry.

Recently, two-dimensional (2D) ternary metal chalcogenides with atomically thin layered structure have emerged as prominent candidates for wide applications in photocatalysis due to their distinctive optoelectronic and photochemical features.[12,13] Notably, incessant efforts have been devoted to developing few-layered 2D hexagonal $ZnIn_2S_4$ (ZIS) atomically thin nanosheets, which consist of S–Zn–S–In–S–In–S stacking layers in periodic arrangement.[14,15] Due to the unique properties of confined thickness in atomic layers, few-layered ZIS nanosheets generally exhibit superior HER performance to its bulk counterpart.[16,17] The lower dimensionality of atomically thin photocatalysts could expose larger surface with more adsorption sites.[18] Analogous to the catalytic properties of the MoS_2 layer, the active sites of ZIS atomic layers for HERs mainly locate at the under-coordinated edge sites or precisely the S atoms on the (110) facet.[19] Even so, the utilization of pristine ZIS atomic layers in photocatalytic water splitting without sacrificial reagents remains a nontrivial task due to the relatively inert active sites with sluggish HER kinetics.[20] With this in mind, maneuvering the surface activity of the intrinsic active sites in ZIS atomic layers *via* targeted engineering of H adsorption energy at atomic level for sacrificial agent-free HER applications has become the subject of great interest.

In an effort to achieve this feat, elemental doping into metal chalcogenides is a prevailing scheme to tune the electronic configuration and regulate the charge dynamics of the neighboring S atoms, thus activating these atoms to be favorable for HERs.[21] Heteroatom doping, whether by the means of atomic substitution or interstitial existence, could form an intermediate state *via* orbital hybridization of metal chalcogenides with the foreign dopants.[22,23] Depending on the charge characteristics of the dopants, the new hybridized state could endow higher charge density due to the additional doped overlayer, hence facilitating carrier migration and charge separation.[24] Besides, the presence of new intermediate states near the valence band maximum (VBM) will confer a reduction in band gap and extend the range of photo-responsiveness. Furthermore, the higher electronegativity nature of S atoms in the S–Zn and S–In coordination of hexagonal ZIS will induce accumulation of electrons around the S atoms, resulting in the formation of negatively charged $S^{\delta-}$ centers and large H adsorption–desorption barriers.[25] As stated by the Sabatier principle, the interaction between the reactive sites and adsorbed intermediates should be moderate for high HER activity.[26] In this context, an efficient HER material should render a thermoneutral state for the balanced adsorption and desorption of H.[27] Therefore, the incorporation of guest heteroatoms into hexagonal ZIS is imperative to activate the intrinsic S atomic sites by modulating the adsorption free energy of H (ΔG_{H^*}) to be closer to zero and enhance the reaction kinetics for HERs. However, it is important to employ a non-invasive doping strategy with the optimal degree, as excess doping would severely distort the electronic structure and might encompass the charge recombination center.[28]

Making full use of the lower electronegativity nature of P atoms (2.19) than S atoms (2.55), the frontier orbital energy of the P-doped ZIS atomic layers can be increased with regulated active sites.[29,30] In this contribution, we present the opportune construction of a fine-tuned P-doped 2D hexagonal $ZnIn_2S_4$ atomic layer (ZIS-P) as a single-component photocatalyst to drive HERs with pure water and seawater without using sacrificial reagents. Atomic insights from density functional theory (DFT) disclose the formation of P–In1 coordination in the lattice of ZIS-P with the lowest formation energy (E_f) among the possible interstitial P doping (IPD) and substitutional P doping (SPD) sites, suggesting that S3 atoms are preferable to be substituted by the guest P atoms. Besides, a detailed investigation on the interconnection between the influence of P atoms on the neighboring S2 atoms and the H adsorption free energy is established. The theoretical simulation reveals a ΔG_{H^*} value closer to zero for ZIS-P as compared to ZIS, indicating the H adsorption–desorption barrier has been significantly reduced. On top of that, the electronic band configuration of ZIS-P with a new hybridized state was validated from the upshifting of VBM and Fermi level characterized by UV-Vis, Mott–Schottky measurement and Kelvin probe force microscopy (KPFM). As a result, the best performing sample (ZIS-P200) exhibited visible light-driven H_2 evolution from pure water (1.68 μmol h^{-1}) and 0.5 M NaCl as simulated seawater (1.54 μmol h^{-1}) without any sacrificial reagent, while no activity was observed for the undoped ZIS sample. It is worth mentioning that the application horizon of ZIS-P200 can be extended into sacrificial agent-free photocatalytic HERs from artificial seawater, and the composition is given in Table S1.† Notably, this work offers an H adsorption kinetic-oriented approach for the intrinsic active site modulation of ZIS *via* P doping to regulate the atomic-level reaction dynamics and opens an avenue for direct photocatalytic seawater splitting using metal sulfides under visible light irradiation.

Experimental section

Materials

Zinc chloride, $ZnCl_2$ (≥98%, Merck), indium(III) chloride, $InCl_3$ (98%, Sigma Aldrich), sodium citrate dihydrate, $C_6H_5Na_3O_7 \cdot 2H_2O$ (≥99%, Merck), thioacetamide, C_2H_5NS (≥99%, Nacalai Tesque), ethylene glycol (≥99%, Sigma Aldrich), sodium hypophosphite monohydrate, $NaH_2PO_2 \cdot H_2O$ (≥99%, Sigma Aldrich), sodium chloride, NaCl (≥99%, Sigma Aldrich), and ethanol, C_2H_5OH (Grade AR 96%, Friendemann Schmidt Chemical), were used as received without further purification. Aqua Ocean Reef Plus Marine Salt (Qingdao Sea-Salt Aquarium

Technology) with the salt formulation as tabulated in Table S1† was used as artificial seawater. Deionized (DI) water (resistivity ≥ 18 MΩ cm), obtained using a Millipore Milli-Q water purification system, was used throughout the course of the experiment.

Preparation of $ZnIn_2S_4$ atomic layers

First, $ZnIn_2S_4$ atomic layers were synthesized by a facile hydrothermal method. In a typical synthesis, 0.5 mmol of $ZnCl_2$, 1 mmol of $InCl_3$ and 300 mg of sodium citrate dihydrate were dissolved in 25 mL of DI water and 5 mL of ethylene glycol (EG) by stirring for 30 min. Subsequently, 2 mmol of thioacetamide was added slowly into the solution and further stirred for 30 min. The solution was then transferred into a Teflon-lined stainless-steel autoclave and subjected to a hydrothermal process at 120 °C for 12 h. After cooling to room temperature, the solid was collected *via* centrifugation and washed with ethanol and DI water 3 times each. The resulting yellow product was finally freeze-dried and denoted as ZIS. A control sample of $ZnIn_2S_4$ was prepared using the similar procedure without adding sodium citrate dihydrate and the resulting product was labelled as pristine ZIS.

Preparation of P-doped $ZnIn_2S_4$ atomic layers

P-doped $ZnIn_2S_4$ atomic layers were synthesized by subjecting ZIS to a thermal phosphorization process in a tube furnace. In brief, 100 mg of ZIS and x mg (x = 100, 200 and 300, respectively) of sodium hypophosphite monohydrate were mixed and ground into a fine powder using an agate mortar and pestle. Next, the powder was placed on a quartz boat and calcined at 300 °C for 2 h under an inert N_2 environment. Successively, the solid was collected and washed with ethanol and DI water 3 times each. Finally, the product was freeze-dried and the resulting P-doped samples were denoted as ZIS-Px (x = 100, 200 and 300, respectively).

Material characterization

The structural, surface morphology and elemental composition of the as-synthesized samples were characterized using a field emission scanning electron microscope (FESEM; Hitachi SU8010) and a high-resolution transmission electron microscope (HRTEM; JOEL JEM-2100F) equipped with an energy-dispersive X-ray (EDX) spectrometer. Meanwhile, the topography and surface potential of ZIS and ZIS-P200 were obtained using an atomic force microscope (AFM; Bruker Multimode 8). The specimens for the AFM electrical mode were prepared by spray coating the sample suspensions, which were pre-dispersed in an ethanol/Nafion solution on a fluorine-doped tin oxide (FTO) glass substrate with a defined area. The as-prepared specimens were then mounted on the AFM sample stage using silver paste for an uninterrupted electrical connection. Besides, the crystallographic properties were determined by X-ray diffraction (XRD) analysis using a Bruker D8 Discover X-ray diffractometer with Ni-filtered Cu Kα radiation at a scan rate of 0.02° s^{-1}. X-ray photoelectron spectroscopy (XPS) measurements were carried out using a Phoibos 100 spectrometer (SPECS, Germany) with a monochromatic Al-Kα X-ray source. Prior to deconvolution, all binding energies were referenced to an adventitious carbon signal (C 1s peak) at 284.6 eV. UV-Vis diffused reflectance spectra (UV-Vis DRS) of the samples were recorded using a Cary 100 UV-Vis spectrophotometer (Agilent) equipped with an integrated sphere and $BaSO_4$ was used as a reflectance standard. Furthermore, steady-state photoluminescence (PL) spectra were recorded using a fluorescence spectrometer (PerkinElmer LS55). Lastly, time-resolved PL (TRPL) spectra were recorded using a DeltaPro Fluorescence lifetime system (Horiba Scientific) at an excitation wavelength of 317 nm.

Electrochemical analysis

Electrochemical analysis (transient photocurrent density, current–potential, Nyquist and Mott–Schottky plots) was performed using a CHI 6005E electrochemical workstation in a conventional three-electrode photoelectrochemical (PEC) setup. The working electrodes were prepared by spray-coating the ethanol/Nafion suspension with dispersed samples onto a FTO glass substrate with an active area of 1 cm^2. Furthermore, Pt was utilized as the counter electrode while Ag/AgCl saturated with 3 M KCl was used as the reference electrode. During the measurements, a 0.5 M Na_2SO_4 aqueous solution was employed as the electrolyte and the working electrode was illuminated by a Xe arc lamp equipped with an optical filter (λ > 400 nm) with a fixed lamp-to-sample distance of 15 cm. The current–potential curve was measured across a bias voltage of 0–1 V at a scan rate of 10 mV s^{-1}, while long-term transient photocurrent density was evaluated at a bias voltage of 0.1 V. Besides, Nyquist plot measurement was conducted in the frequency range of 0.1–10^5 Hz at an applied potential of 0.4 V. In addition, the Mott–Schottky plot was constructed in the potential range of −2 to 1 V at a frequency of 1000 Hz.

Computational methods

The theoretical calculations were performed using density functional theory (DFT) *via* the generalization-gradient approximation (GGA) with the exchange–correlation function of Perdew–Burke–Ernzerhof (PBE).[31] The calculations were implemented using the Vienna *Ab initio* Simulation Package (VASP) with the projector augmented wave (PAW) method, which spanned reciprocal space with plane-wave basis.[32] A plane-wave basis set with an energy cutoff of 500 eV, an energy convergence of 1×10^{-5} eV and a force convergence of 0.01 eV $Å^{-1}$ was used. The Monkhorst–Pack k-point mesh was set at 3 × 3 × 1. An additional vacuum layer of approximately 15 Å was applied to separate possible interactions between the periodic images. Hybrid functional based on the Heyd–Scuseria–Ernzerhof (HSE06) method was adopted to obtain the most stable structure during the relaxation calculations.[33] For interstitial P doping (IPD) calculations, a single P atom was added into the possible interstitial sites of the 1 × 1 atomic bilayer structure, while the intrinsic S atom was replaced with a P atom for the substitutional P doping (SPD) calculations. All model lattice structures were visualized using Visualization for Electronic and Structural Analysis (VESTA).

To determine the favorable atomic form of P doping in ZIS, the formation energy E_f for IPD and SPD were calculated using eqn (1) and (2), where $E_{ZIS\text{-}P}$ and E_{ZIS} are the total energy of P-doped ZIS (ZIS-P) and ZIS; μ_P and μ_S refer to the chemical potential of the P dopant and substituted S atom derived from the bulk phase, respectively. The lowest formation energy calculated corresponds to the most stable and energetically favorable structure.

Interstitial P doping (IPD):

$$E_{f,IPD} = E_{ZIS\text{-}P} - (E_{ZIS} + \mu_P) \quad (1)$$

Substitutional P doping (SPD):

$$E_{f,SPD} = (E_{ZIS\text{-}P} + \mu_S) - (E_{ZIS} + \mu_P) \quad (2)$$

The thermodynamics process of H_2 evolution reactions (HERs) involves the adsorption and binding of H atoms (H*) onto the active sites of the photocatalyst, followed by the desorption of H_2 molecules. Thus, the differential binding energy of H (ΔE_{H^*}) was first calculated using eqn (3), where E_{PC+H}, E_{PC} and E_{H_2} represent the total energy of the photocatalyst with one adsorbed H atom, total energy of photocatalyst without H atoms and energy of gas-phase H_2 molecules, respectively. In addition, the adsorption free energy of H (ΔG_{H^*}) was determined using eqn (4) as the descriptor for HER activity, where ΔZPE refers to the difference in zero-point energy correction for vibration frequency between adsorbed phase (H*) and gas phase (H_2), while $T\Delta S$ denotes the entropy contribution by the adsorption of $\frac{1}{2}H_2$ molecule at temperature T. For metal-based materials, the value of $(\Delta ZPE - T\Delta S)_{H^*}$ can be taken as 0.24 eV.

Differential binding energy of H:

$$\Delta E_{H^*} = E_{PC+H} - \left(E_{PC} + \frac{1}{2}E_{H_2}\right) \quad (3)$$

Adsorption free energy of H*:

$$\Delta G_{H^*} = \Delta E_{H^*} + (\Delta ZPE - T\Delta S)_{H^*} \quad (4)$$

Evaluation of photocatalytic activities

The photocatalytic water splitting reaction was conducted in a Pyrex top-irradiated vessel with quartz window under continuous N_2 flow at atmospheric pressure. Each photocatalyst sample (0.03 g) was dispersed in 60 mL of: (i) pure water, (ii) 0.5 M NaCl as simulated seawater and (iii) aqueous solution containing 2 g of sea salt as artificial seawater (composition as formulated in Table S1†) without using any sacrificial reagent and pH adjustment. Prior to the photocatalytic activity, the reaction system was evacuated by purging N_2 gas at a high flow rate for 30 min. A 350 W Xe arc lamp equipped with an optical filter (λ > 400 nm, intensity = 100 mW cm^{-2}) was used as a visible light source. The gas sampling port of the system is directly connected to a gas chromatograph (Agilent 7820A, TCD, Ar carrier gas) for measuring the product gas online at an hourly auto sampling interval. The apparent quantum yield (AQY) was calculated by evaluating the photocatalytic H_2 evolution under monochromatic light using a 420 nm band pass filter, according to eqn (5).

$$AQY = \frac{2 \times \text{number of evolved } H_2 \text{ molecules}}{\text{number of incident photons}} \times 100\% = \frac{2vtN_A}{IS t\lambda\left(\frac{1}{hc}\right)} \times 100\% \quad (5)$$

where v = H_2 rate (mol s^{-1}), t = reaction time (s), N_A = Avogadro's constant (mol^{-1}), I = light intensity (W cm^{-2}), S = irradiation area (cm^2), λ = wavelength of incident light (nm), h = Planck constant (J s) and c = speed of light (nm s^{-1}).

On top of that, a $^{\bullet}$OH radical trapping test was conducted *via* PL technique by using terephthalic acid (TA) as a probe molecule. The experimental methods were identical to the photocatalytic water splitting reaction with the addition of 5 mM TA aqueous solution adjusted by 10 mM NaOH. The PL spectra were recorded using a fluorescence spectrometer (PerkinElmer LS55) at an excitation wavelength of 315 nm.

Results and discussion

Material design and structural characterization

Two-dimensional (2D) hexagonal ZIS atomic layers with various degrees of P doping were prepared *via* a simple two-step hydrothermal and phosphorization route. The surface morphology and microstructures of the as-synthesized samples were first analyzed by TEM and HRTEM. As depicted by the TEM image in Fig. 1a, ZIS renders a translucent and ultrathin sheet-like morphology with a lateral dimension of several hundreds of nanometers. With the addition of sodium citrate dihydrate as a surfactant, ZIS embodies a clean and freestanding few-layered structure in stark contrast to the aggregated micron-size morphology of pristine ZIS composed of plenty of intersecting nanosheets (Fig. S1†). The increase in the edge exposure of ZIS atomic layers is beneficial for unveiling the active surface. Fig. 1b shows the HRTEM image of ZIS, revealing clear lattice stripes with an interplanar distance of 0.33 nm, which corresponds to the (100) orientation of hexagonal ZIS.[28] A close observation on the lattice fringes of ZIS uncovers an interaxial angle of 120°, which substantiates the hexagonal phase of the crystal structure.[21] Besides, the elemental composition of ZIS was further divulged *via* a false-colored STEM image and EDX mapping, which show the homogeneous distribution of Zn, In and S elements (Fig. 1c–e). Furthermore, ZIS-P200 exhibits similar morphology and microstructures as ZIS, thus suggesting that the P-doped sample retains the hexagonal domain (Fig. 1f and g). Particularly, ZIS-P200 possesses a lattice interspacing of 0.34 nm, indicating the slight expansion in lattice after P doping. Furthermore, both ZIS and ZIS-P200 have good crystalline structures as there are no discontinued lattice fringes. The false-colored image and EDX mapping of ZIS-P200 show the existence of heteroatom P in the crystal framework with a fairly uniform distribution (Fig. 1h and i). The degree of P doping

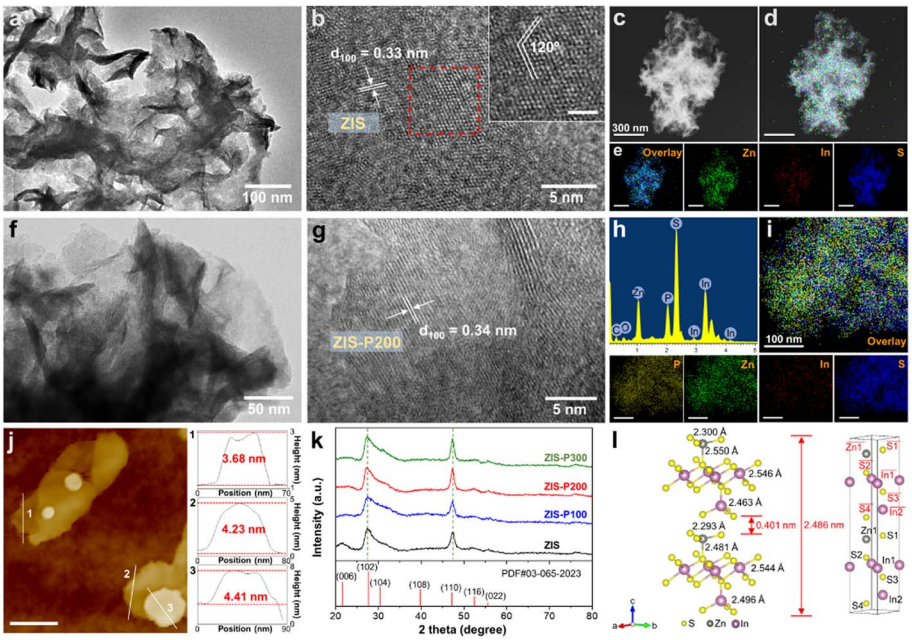

Fig. 1 Morphology and composition characterization. (a) Representative TEM and (b) HRTEM images of ZIS (scale bar of inset: 2 nm). (c) STEM image and corresponding (d) false-colored image and (e) EDX elemental mapping of ZIS (scale bar: 300 nm). (f) Representative TEM and (g) HRTEM images of ZIS-P200. (h) EDX spectrum and (i) elemental mapping of ZIS-P200 (scale bar: 100 nm). (j) AFM image and corresponding height profiles of ZIS-P200 (scale bar: 200 nm). (k) XRD patterns of the respective samples. (l) Crystal structure of the hexagonal ZIS bilayer with dimensions (left) and bond exclusion model with atom labelling for visualization (right).

ranging from 3.08 to 10.89 at% for the P-incorporated samples was measured from EDX analysis, as tabulated in Table S2.†

The thickness of the atomic layers was then attained *via* AFM measurement. Fig. 1j delineates the representative AFM topography image and the corresponding height profiles across three selected areas of the ZIS-P200 sample. It can be clearly visualized that ZIS-P200 atomic layers confer an average topographic height of 4.11 nm, which is equivalent to *ca.* one and a half unit cell thickness of the ZIS bilayer slab.[34] Besides, ZIS renders a height profile ranging from 3.43 nm to 4.81 nm (Fig. S2†). This result manifests the few-atomic thin nature of the as-synthesized samples with 2D morphology, attributed to the employment of sodium citrate dihydrate as the surfactant. On top of that, the crystallographic and phase structures of ZIS and the P-doped samples were obtained by XRD analysis. As shown in Fig. 1k, all the samples display characteristic peaks, which are indexed to the hexagonal structure of ZIS with major diffraction peaks at 27.6° and 47.2° corresponding to the (102) and (110) crystal planes, respectively (JCPSD no. 65-2023).[35] It is worth noting that the XRD patterns of the P-doped samples are consistent with ZIS, reflecting that the crystal phases of the hexagonal domain remain dominantly unchanged with the absence of impurity phase after the introduction of heteroatom dopants. Besides, careful observation shows that the peak positions of the two major peaks corresponding to the (102) and (110) planes are slightly shifted to lower diffraction angles, specifying a modest lattice expansion after the incorporation of P atoms into the hexagonal ZIS structure, which increases the lattice parameters (Fig. S3†). The theoretical model of one-unit-cell ZIS is depicted in Fig. 1l. The simulated crystal structure of hexagonal ZIS is composed of bilayer configuration with identical arrangement of atoms at the top and bottom layers. It should be mindful that the bond lengths of the metal-S coordination at the top layer (*i.e.*, $\overline{\text{Zn1}} - \overline{\text{S1}}$) and the bottom layer (*i.e.*, Zn1–S1) are different owing to the potential interactions across the interlayer spacing.

XPS was then applied to elucidate the chemical composition and valence states of the constituent elements in the samples by taking the C 1s peak as the calibration reference. The presence of P coexists with Zn, In and S, as the major elements with no adventitious foreign impurities in ZIS-P200 can be detected from the full XPS survey spectra (Fig. S4†). Based on Fig. 2a and b, the Zn 2p orbital components of ZIS are split into Zn $2p_{3/2}$ (1021.95 eV) and Zn $2p_{1/2}$ (1045.01 eV), while the In XPS peaks at 444.93 and 452.52 eV correspond to the In $3d_{5/2}$ and In $3d_{3/2}$ transitions. Besides, two deconvoluted S 2p XPS peaks of ZIS centered at 161.89 and 162.99 eV were assigned to the spin–orbit splitting of S $2p_{3/2}$ and S $2p_{1/2}$ (Fig. 2c). Notably, the S $2p_{3/2}$ and S $2p_{1/2}$ XPS peaks of ZIS-P200 evidently shifted to lower binding energies, revealing the generation of subtle S vacancies upon substitutional P doping. Owing to the lower electronegativity nature of P dopants, the equilibrium electron cloud density of S atoms is higher in ZIS-P200, which leads to a decrease in the binding energy of S 2p.[35] These findings are in good agreement with the slight negative shifting of Zn 2p and In 3d XPS peaks in ZIS-P200 as compared to ZIS since the P-induced S vacancies would decrease the coordination number of Zn and In, which, in turn, reduces the metal cations to lower

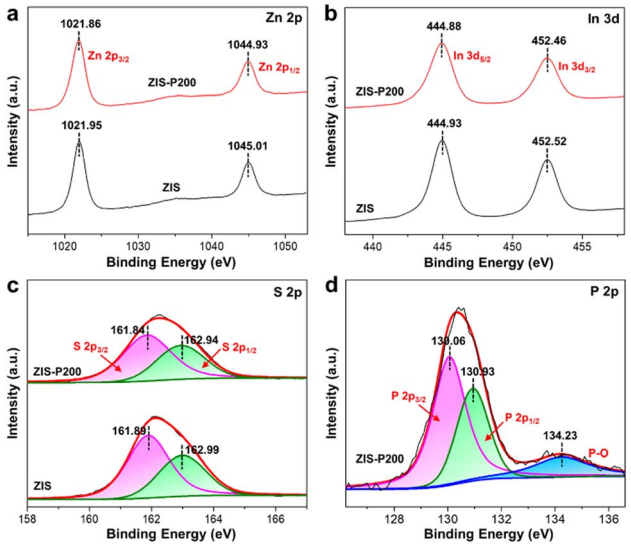

Fig. 2 XPS spectra. (a) Zn 2p, (b) In 3d and (c) S 2p XPS spectra of ZIS and ZIS-P200. (d) P 2p XPS spectra of ZIS-P200.

valence states.[36] Furthermore, the doping nature and configuration of P atoms of ZIS-P200 are depicted in the P 2p XPS spectra (Fig. 2d), disclosing three peaks at 130.06, 130.93 and 134.23 eV indexed to P $2p_{3/2}$, P $2p_{1/2}$ and surface-oxidized P species respectively. Thus, it can be concluded that P atoms have been successfully incorporated into the framework of ZIS. In an effort to probe the effect of P content in ZIS, the XPS spectra of ZIS-P100 and ZIS-P300 were recorded and are shown in Fig. S5.† It can be noticed from Fig. S5d† that the higher degree of P doping in ZIS increases the intensity of P $2p_{3/2}$ and P $2p_{1/2}$ peaks. Similar to ZIS-P200, both Zn 2p and In 3d peaks of ZIS-P100 and ZIS-P300 samples display a slight shifting to a low binding energy in relation to ZIS (Fig. S5a and b†). In this context, the results reveal that the metal cations are at lower valence states and accretive negative charges were redistributed around S atoms in the ZIS samples with the increase in P content, as evidenced from the stepwise decrease in the S 2p binding energy (Fig. 2c and S5c†). Moreover, the elemental compositions of ZIS and ZIS-P200 obtained from the XPS measurements are tabulated in Table S3,† unfolding a transition of Zn : In : S molar ratio from 1 : 2 : 4 to 1 : 2 : 4 − x. This corroborates the presence of S vacancies in ZIS induced by the substitutional doping of heteroatom P.

Insights into optoelectronic properties and H adsorption energy

Other than the alteration in structural and chemical properties, the influence of substitutional P doping on the optoelectronic properties of ZIS, for instance, light absorption capabilities, charge transport kinetics and electronic band symmetry, is of utmost important to be investigated. Band structure characterization was employed to provide a discerning understanding of the interrelation between the degree of P content and the variation in the relevant energy levels. The light absorption characteristics of the samples are manifested from the UV-Vis

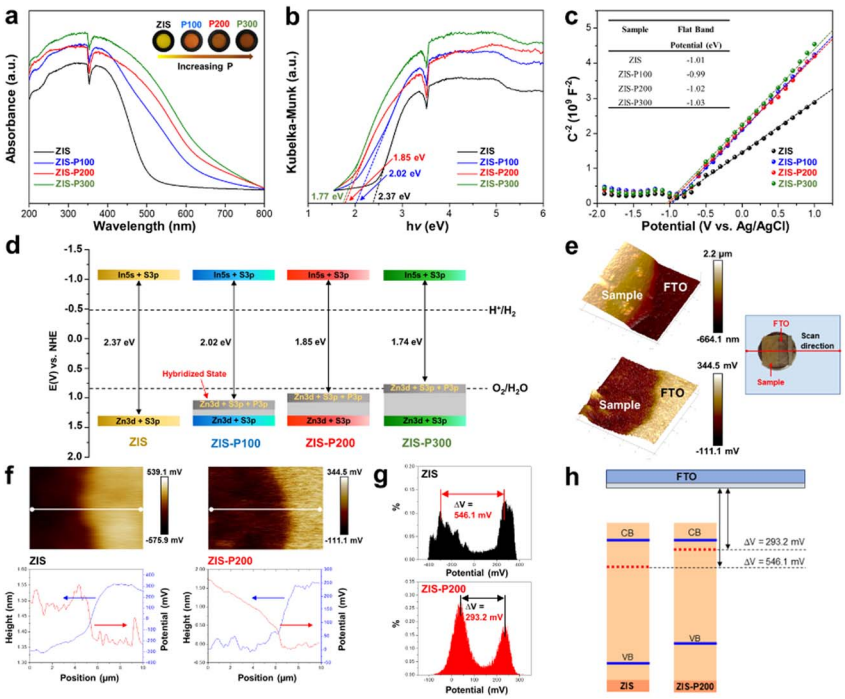

Fig. 3 Optoelectronic properties and band structure characterization. (a) UV-Vis DRS of the respective samples (inset shows the color changes of the samples with the increase in P doping). (b) Plots of transformed KM function. (c) Mott–Schottky plots and (d) relative band structure diagram of the respective samples. (e) Three-dimensional topography image (top) and corresponding Kelvin probe data, *i.e.*, potential map (bottom) at the ZIS-P200/FTO boundary. (f) Topography and potential profiles of ZIS and ZIS-P200 (white line indicates the scan direction). (g) Histogram analysis of the acquired Kelvin probe data. (h) Schematic of the estimated WF positions of ZIS and ZIS-P200 in relation to FTO.

DRS shown in Fig. 3a. Gradual red-shifting of the absorption edges is perceived with the increasing extent of P doping into ZIS. Besides, the enhanced background absorption of ZIS-P in the visible region is ascribed to the band trailing effect induced by S vacancies associated with the substitutional P atoms, which can be further validated by the gradual color change from yellow to dark brown for the samples with a higher P loading (inset of Fig. 3a). According to the plots of transformed Kubelka–Munk (KM) function shown in Fig. 3b, the band gap of ZIS was found to be reduced after P doping, and hence, it can be reckoned that the improvement of light harvesting abilities of ZIS is in conjunction with the increase in P contents. Subsequently, the flat-band information of the samples was acquired by the Mott–Schottky (M–S) analysis. As shown in Fig. 3c, all the samples render positive slopes in the M–S plots, which resemble n-type semiconductor behaviors.[37] By extrapolating the slopes of the M–S plots, the flat-band potentials of ZIS and ZIS-P samples were identified to be in the narrow range of −0.99 to −1.03 eV with reference to the Ag/AgCl electrode. As widely accepted, the CBM potential of the n-type semiconductor was estimated to be −0.2 V than its flat-band.[38] Based on the principle for energy level conversion, *i.e.*, E(V) *vs.* NHE = E(V) *vs.* Ag/AgCl + 0.197 V, the CBM energy level of the samples with respect to NHE can be approximated to their flat-band values from the M–S graph.[39,40] The relative band structure diagrams of the samples are then postulated in Fig. 3d. On account of the flat-band values in close vicinity to each other, the CBM of the samples is relatively unchanged after P doping. Thus, it can be speculated that the narrowing in band gap of ZIS with the increase in P doping is primarily correlated with the formation of new hybridized states that upshift the VBM. In this regard, all the samples feature a strong reduction potential due to high CBM energy levels. However, an extensive degree of P doping in ZIS (ZIS-P300) resulted in the strong elevation displacement of VBM, which, in turn, hampers the oxidation capabilities.

Work function (WF) is another important indicator in reflecting the free electron dynamics of semiconductors and unambiguously related to the photocatalytic performance.[41] To predict the changes in WF between ZIS and ZIS-P200, the employment of Kelvin probe force microscopy (KPFM) in determining the contact potential difference (CPD) between the samples and a conductive reference (*i.e.* FTO) using an AFM electrical mode was performed. As presented in the inset of Fig. 3e, the specimens with a defined sample-FTO area were prepared *via* spray coating and were electrically connected to the AFM sample stage using silver paste. When a biased AFM probe was swept across an x–y scan area of the sample-FTO boundary, the surface topography of the sample and its corresponding CPD values that originated from the bias voltage in neutralizing the electric field were recorded simultaneously.[42,43] As a result, the Kelvin probe data, *i.e.*, CPD can be acquired as a function of position, which enables a direct mapping of surface potential of the sample along the third dimension (z-axis). Fig. 3e delineates the 3D topography image (top) and the corresponding surface potential map (bottom) across the interface of ZIS-P200 and FTO. A step decrease in the height profile is observed at the sample-FTO border. This transition in topography is translated into the potential profile with a step increase in CPD. Besides, the individual topography and potential profiles of the line scan (indicated by the white line in the 2D potential images) for ZIS and ZIS-P200 are depicted in Fig. 3f. It can be clearly noticed that the transition in height and potential steps consistently occurs at the same position, indicating the frontier of the two distinct materials. On top of that, Gaussian fitting of the histogram analysis on the Kelvin probe data shows two prominent peaks, which represent the average CPD difference between the sample and FTO, namely, ΔV (Fig. 3g). In this context, ZIS-P200 renders a much lower ΔV value (293.2 mV) in contrast to ZIS (546.1 mV), signifying a reduction of WF after P doping. Even so, the absolute WF values of the samples could not be attained since the KPFM measurements were conducted under ambient conditions. Therefore, FTO was utilized as a conductive reference to precisely estimate the local variation of WF across the sample/FTO boundary. This technique bestows a viable approach to compare the relativity of WF between samples. Fig. 3h reveals the changes in the relative WF of ZIS after P doping, unravelling the upshifting of the Fermi level to a more electronegative energy due to the formation of hybridized state. Principally, semiconductors with a higher Fermi level can facilitate the electron transition and provide more photogenerated electrons to CBM, thus endowing a larger driving force for HERs.[44,45] With respect to this, the amplitude of Fermi level elevation is unambiguously correlated with the performance of HERs.

To gain an atomic insight into the doping behavior of P atoms in ZIS and further probe its modulation effect on the crystal structures, electronic properties and H adsorption kinetics, first-principles calculations *via* density functional theory (DFT) were conducted. Two different doping scenarios, namely, interstitial P doping (IPD) and substitutional P doping (SPD), were considered during the calculations. Fig. 4a illustrates the four possible doping sites for IPD and SPD. In the case of SPD, S atoms are more likely to be replaced by P dopants as compared to Zn and In due to the relatively close electronegativity and atomic radius of S and P atoms.[29,46] According to Fig. 4b, the calculated formation energies (E_f) of the four selected sites are in the negative range, implying that all the IPD and SPD are energetically plausible. Specially, the E_f values for SPD are much lower than that of the IPD structures, indicating that the P doping in ZIS is preferable to be in substitutional rather than interstitial form. In this regard, ZIS-P with SPD at site 3 displays the lowest E_f value (−2.082 eV), which corresponds to the most stable and energetically favorable structure. Thus, S3 atoms in ZIS are most likely to be substituted upon P doping, which break the intrinsic In–S bonds, leading to the formation of new P–In coordination in the lattice. These findings ascertain the lattice expansion phenomena observed from the HRTEM and XRD measurements since the inlaid P atoms have a larger atomic radius than that of S atoms. Besides, significant distortions can be noticed on the IPD atomic structures, while the SPD models experience tenuous distortion.

The subsequent DFT calculations on the investigation of the inherent correlation between the electronic nature and HER energetics were performed using ZIS-P with SPD at site 3 model.

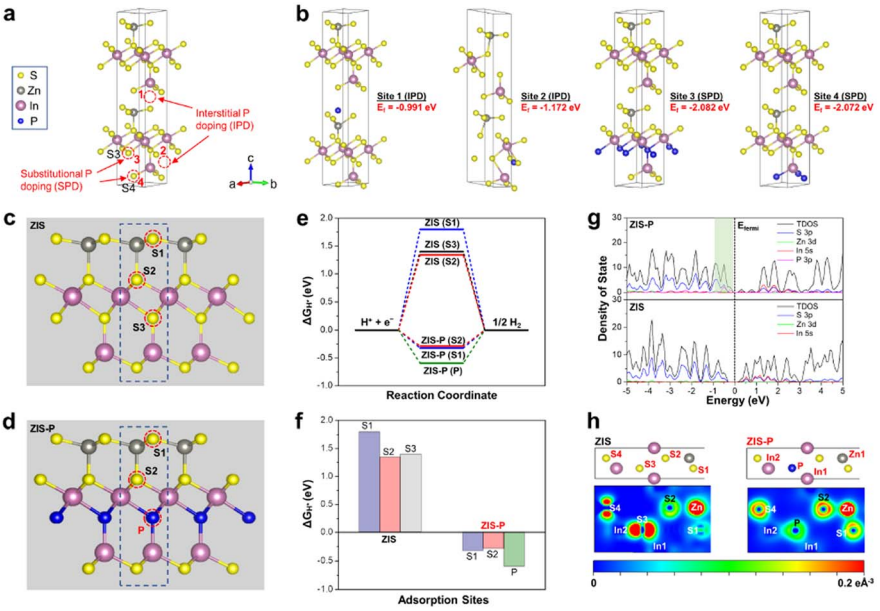

Fig. 4 Influence of P doping on the crystal structures, electronic properties and H adsorption kinetics of ZIS. (a) Crystal structure model of ZIS with different possible interstitial and substitutional P doping sites. (b) Optimized crystal structure of P-doped models with the respective formation energy per atom (E_f). Position of possible active sites for (c) ZIS and (d) ZIS-P (SPD at site 3). (e) Calculated adsorption free energy diagram and (f) the corresponding adsorption free energy values of H on different atomic sites for ZIS and ZIS-P (SPD at site 3). (g) Calculated density of states (DOSs) of ZIS and ZIS-P (SPD at site 3). Light green shading indicates the increase in DOS at VBM after P doping. (h) Monolayer structures of ZIS and ZIS-P (SPD at site 3) with their respective charge density distribution along (110).

The calculated density of states (DOS) of ZIS discloses that the VBM is mainly contributed by Zn 3d and S 3p orbitals, whereas the conduction band minimum (CBM) comprises In 5s and S 3p orbitals (Fig. 4g). Since heteroatom P has lower valence electrons ($3s^2 3p^3$) than those of the substituted S atoms ($3s^2 3p^4$), an unoccupied valence orbital is formed upon doping.[47] Thus, an upshifting of VBM can be observed in the DOS of ZIS-P due to the formation of new hybridized electronic states associated with the additional P 3p orbital, accompanied by a significant increase in the electron density (shown in the light green shading of Fig. 4g). As the CBM remains unchanged, ZIS-P endows a reduction in band gap with an elevation of the Fermi level. The presence of new hybridized electronic states near the VBM could impart ZIS-P with enhanced metallic conductivity attributes, which facilitate the charge dynamics and hinder the recombination of photogenerated carriers.[48] The H adsorption free energy (ΔG_{H^*}) was then calculated as a crucial descriptor for the H adsorption–desorption barrier to further evaluate the potential HER activity of ZIS after P doping. According to the Sabatier principle, an ideal HER material should render thermoneutral nature for the binding of intermediates with the active surface.[49] A near-zero value of ΔG_{H^*} is correlated with the decrease in the reaction barriers as both adsorption and desorption steps are better compromised, leading to the enhanced HER kinetics.[50] The H adsorption behavior was modelled over three possible active sites for each sample, namely: (1) S1 atom, (2) S2 atom and (3) the SPD site (S3 for ZIS and P for ZIS-P), as shown in Fig. 4c and d. Based on Fig. 4e, it can be deduced that S1 and S3 atoms of ZIS are the less conducive HER active sites since the ΔG_{H^*} values are the furthest from zero while the S2 atom is more favorable. However, they are still far from the thermoneutral states. The significantly positive ΔG_{H^*} values on the S atomic sites of ZIS imply the weak adsorption of H, implying that the surface is relatively inert for HERs. On the polar opposite, the introduction of P dopants can fine-tune the binding energies of H adsorption–desorption step on the S1 and S2 atomic sites of ZIS and greatly reduce the energy barrier along the reaction coordinate, hence activating the surface for HERs (Fig. 4e). In particular, the close to thermoneutrality of H adsorption energy insinuates that the S2 sites of ZIS-P become the most favorable sites for HERs after P modulation (Fig. 4f). This affirms that the introduction of P atoms can regulate the electronic properties and balance the H adsorption states of the neighboring S atoms to be active for HERs. Moreover, the "states-filling" effect from the hybridized states can accept the electrons from H*, which decrease the energy required to accommodate the H electron, resulting in a lower H adsorption–desorption barrier.[51] The relationship between the H adsorption kinetics and the electronic structure is further attested by the charge density distribution simulation. Fig. 4h illustrates the charge density distribution around the atoms in ZIS and ZIS-P at the surface of the doped layer. It is apparent that S1 and S2 atoms of ZIS possess low charge density before P doping. According to the formation energy calculations, the S3 atom is most favorable to be substituted upon the intrusion of P atoms. In this case, the presence of P atoms with different valence electrons and atomic electronegativity can induce redistribution of electrons within

the local coordination, hence modulating the charge density of the neighboring S atoms and synergistically regulating the H adsorption, as evidenced from the higher charge densities of S1 and S2 atoms after P doping. Particularly, the charge distribution around the S2 atom increases drastically, indicating that the substitutional P atom could activate the idle plane into potential HER active sites. These findings are in good agreement with the close to thermoneutral states of H adsorption free energy on S2 atoms of ZIS-P, which enables energetically favorable HERs.

Photocatalytic H_2 evolution from pure water and seawater

The photocatalytic HER performance of the samples was first evaluated *via* visible-light-driven pure water splitting without any sacrificial reagent. As shown in Fig. 5a, the photocatalytic HER activities were observed to follow an increasing trend when the content of P dopants in ZIS is increased from 3.08 at% (ZIS-P100) to 6.97 at% (ZIS-P200). Particularly, the best performing sample (ZIS-P200) exhibited a remarkable photocatalytic H_2 evolution rate of 1.68 μmol h^{-1} from pure water, unfolding the significance of active site modulation by the optimal degree of substitutional P doping for a decreasing H adsorption–desorption barrier with the enhanced HER kinetics (Fig. 5b). It should also be noted that ZIS did not deliver any appreciable H_2 yield mainly due to the relatively inert S atomic sites as evidenced from the highly positive H adsorption free energy (Fig. 4e), leading to sluggish HER kinetics in pure water. In contrast, ZIS engineered with P dopants demonstrated an outstanding H_2 yield under sacrificial agent-free conditions imputed to the overall synergistic effect from the new hybridized state that upshifts the VBM and Fermi level, leading to enhanced light absorption and accelerated electron transition. The apparent quantum yield (AQY) of ZIS-P200 for H_2 evolution was measured to be 0.16% under 420 nm monochromatic light irradiation. However, the photocatalytic HER performance of ZIS-P300 deteriorates as compared to ZIS-P200 due to the heavy upshifting of VBM associated with excessive doping, which, in turn, distorts the electronic configuration and weakens the oxidation potential counterpart.

Besides, it is worth noting that the application horizon of the P-doped ZIS samples can be extended into photocatalytic HERs from seawater splitting. Since the major components in natural seawater are predominantly composed of sodium (Na^+) and chloride (Cl^-) ions, visible light-driven photocatalytic seawater splitting was initially executed using a 0.5 M NaCl aqueous solution as simulated seawater. As delineated in Fig. 5b, the trend of photocatalytic HER performance of the P-doped ZIS samples in 0.5 M NaCl is analogous to the pure water splitting results. However, a slight reduction in the H_2 yield of simulated seawater splitting is mainly due to the presence of excessive NaCl that imposes adsorption inhibition of reactants associated with the formation of a salt layer over the photocatalyst surface

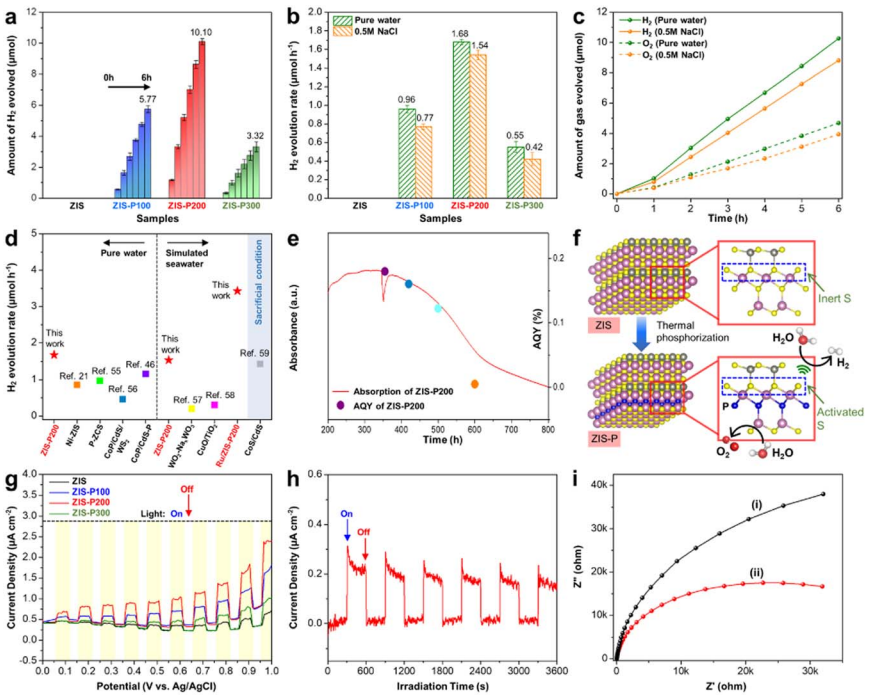

Fig. 5 Photocatalytic H_2 performance and electrochemical measurements. (a) Time courses of H_2 evolution of the respective samples in pure water under visible light irradiation. (b) H_2 yield in pure water and 0.5 M NaCl as simulated seawater under visible light irradiation. (c) Time courses of H_2 and O_2 evolution of ZIS-P200 in pure water and simulated seawater under visible light irradiation. (d) Comparison of photocatalytic HER performance from pure water and simulated seawater for ZIS-P200 with other reported works (shaded region shows the reported work in the sacrificial agent-driven HER). (e) UV-Vis DRS and wavelength-dependent AQY of ZIS-P200 in pure water. (f) Schematic of the photocatalytic H_2O reduction into H_2 on the S atomic active sites of ZIS and ZIS-P. (g) Current–potential curves of the respective samples under intermittent visible light irradiation. (h) Long-term transient photocurrent response of ZIS-P200. (i) Nyquist impedance plots of (i) ZIS and (ii) ZIS-P200.

that hinders the transmission of photogenerated charge carriers.[52,53] Even so, ZIS-P200 still demonstrated an exceptional H_2 yield of 1.54 μmol h^{-1} in simulated seawater under visible light irradiation. Similarly, no activity was observed for the ZIS sample due to its incompetency to drive HERs without any sacrificial reagent. On top of that, O_2 gas was detected in close to stoichiometric value of 1 : 2 with H_2 for ZIS-P200 in both pure water and simulated seawater (Fig. 5c). In order to further substantiate the kinetically facile photocatalytic water oxidation route of ZIS-P200, terephthalic acid (TA) in the basic solution was used as a probe molecule for the ˙OH radical trapping test. The presence of ˙OH can be detected by photoluminescence (PL) measurement since the radical will react with TA to form a fluorescent product – 2-hydroxyterephthalic acid with a PL signal of 425 nm.[54] Fig. S6a and b† show that the PL intensity increases over time for the photocatalytic reaction of ZIS-P200 in both pure water and simulated seawater, implying the generation of OH *via* single-electron oxidation of water.

A comparison of the photocatalytic HER performance from pure water and simulated seawater of ZIS-P200 with other reported works is depicted in Fig. 5d.[21,46,55–59] In terms of pure water conditions, ZIS-P200 exhibits a much higher photocatalytic H_2 evolution rate than that of other co-catalyst-free metal chalcogenide-based single-component photocatalysts and the H_2 yield is even comparable with the co-catalyst-loaded systems (Table S4†). Moreover, the amount of H_2 generated by ZIS-P200 from simulated seawater without any sacrificial reagent far exceeds majority of the previously reported non-metal chalcogenide photocatalysts. Furthermore, ZIS-P200 loaded with 0.5 wt% Ru is also provided for comparison. In spite of that, the research of metal chalcogenides in photocatalytic HERs from seawater without any sacrificial reagent is relatively untouched. Thus, the photocatalytic HER performance of other reported metal chalcogenides with co-catalysts in the presence of sacrificial reagents is presented in the shaded region of Fig. 5d as a reference. Apart from that, the photocatalytic HER performance of the best sample (ZIS-P200) was tested using artificial seawater as the reaction medium. As displayed in Fig. S6c and d,† ZIS-P200 exhibited sacrificial agent-free photocatalytic HERs in artificial seawater, resulting in a H_2 evolution rate of 0.72 μmol h^{-1}. By having a side-by-side comparison of photocatalytic water splitting performance in different reaction media, the H_2 evolution rates of ZIS-P200 were found to be in the order of pure water > 0.5 M NaCl (simulated seawater) > artificial seawater. This is owing to the presence of detrimental chlorine chemistry in complex cation environment of artificial seawater that can significantly hamper the HER activity. Interestingly, no H_2 result was detected for ZIS samples without P doping under all the reaction conditions, which further evidence the importance of heteroatom engineering to drive water splitting in a sacrificial agent-free environment.

On top of that, the photocatalytic performance of ZIS-P200 under full-spectrum irradiation was also recorded (Fig. S7a and b†). In this regard, ZIS-P200 demonstrates an exceptional H_2 evolution rate up to 2.66 and 2.39 μmol h^{-1} in pure water and simulated seawater, respectively. Furthermore, Fig. 5e shows the consistency between the optical absorption behavior of ZIS-P200 and its AQY at different wavelengths, which affirms that the HER activities are driven by the light harvesting ability of the photocatalyst. In addition, it is noteworthy that ZIS-P200 maintained a photocatalytic activity of 81.6% after three successive cycles in pure water, indicating that the sample renders high photostability (Fig. S7c†). As disclosed by the TEM image and XRD patterns in Fig. S8a and b† respectively, there is a negligible change in the morphology and crystal structure of ZIS-P200 after 18 h of photocatalytic reaction in pure water. Besides, the chemical composition of ZIS-P200 displays a marginal difference after the stability test (Fig. S8c, d and Table S5†). Furthermore, ZIS-P200 retained an activity of 68.1% after three photocatalytic cycles in simulated seawater owing to the adsorption inhibitory effect from excessive NaCl (Fig. S7d†). In this context, the S content of the recycled sample is slightly lower after the reaction in simulated seawater than in pure water due to the more inferior photocatalytic stability in a complex medium (Table S5†). Additionally, the possibility of the backward reaction of ZIS-P200 in pure water was investigated *via* a H_2–O_2 recombination testing (Fig. S9†). A gradual increase in H_2 yield is observed under visible light irradiation, followed by a slight decrease in evolved gas and maintained at a relatively similar value when the light source is removed. This infers the occurrence of H_2–O_2 recombination reaction but in a trivial manner. Fig. 5f shows the plausible photocatalytic HER mechanism in ZIS before and after P doping. The presence of heteroatom P can activate the inert intrinsic S atoms in ZIS, thus facilitating the HER kinetics with a thermoneutral H adsorption state.

The charge transfer kinetics of the samples was further ascertained by photoelectrochemical measurements. As revealed by the current–potential (*I*–*V*) curves in Fig. 5g, ZIS and P-doped ZIS samples exhibit anodic photocurrent, which well reflects their n-type semiconducting nature. In particular, ZIS-P200 displays a distinct augmentation in photocurrent density in contrast to ZIS across a bias voltage of 0–1 V under intermittent light illumination. In general, a stronger intensity of photocurrent corresponds to a higher efficiency of charge separation and transfer, which can be regarded as a direct reflection of photocatalytic performance.[60–62] Besides, ZIS-P200 manifests high photocurrent stability under long-term chronoamperometry at a bias voltage of 0.1 V (Fig. 5h). Furthermore, the charge transfer resistance at the electrode/electrolyte interface is reflected by the arc radius of the EIS Nyquist plot. A more depressed semicircle of ZIS-P200 than that of ZIS in the EIS Nyquist plot indicates a lower resistance with the accelerated charge transfer process (Fig. 5i).[63,64] In addition, the radiative recombination of the photoinduced charges was verified using steady-state PL analysis as the intensity of PL mirrors the probability of charge recombination.[65] As shown in Fig. S10a,† ZIS-P200 confers a weakened PL intensity as opposed to ZIS, suggesting that the electron relaying process in ZIS-P200 is a facile transport with the suppression of electron–hole pair recombination. Time-resolved PL (TRPL) was then carried out to investigate the fluorescence decay lifetime of the charge carrier dynamics. As depicted in Fig. S10b,† the fluorescence decay

curves of ZIS and ZIS-P200 can be well fitted to a standard bi-exponent function of $I(t) = A + B_1\exp\frac{-t}{\tau_1} + B_2\exp\frac{-t}{\tau_2}$, where B and τ denote the relative amplitude and lifetime respectively.[65] In this case, ZIS-P200 confers an average lifetime τ of 2.01 ns, which is apparently longer than ZIS with τ of 0.62 ns. Thus, it can be deduced that the presence of new hybridized state imparts ZIS-P200 with amplified metallic conductivity and higher electron density, leading to the enhanced charge dynamics and efficient electron–hole separation.

Conclusions

In summary, we have successfully demonstrated that the active sites of 2D hexagonal $ZnIn_2S_4$ atomic layers (ZIS) could be modulated *via* atomic P doping to achieve sacrificial agent-free photocatalytic HERs from both pure water and seawater. Theoretical insights from DFT calculations disclose that the incorporation of substitutional P atoms into ZIS would form a new hybridized state that prompts the upshifting of VBM and Fermi level, resulting in the reduction of band gap and facilitation of the electron transition with the enhanced HER kinetics. Besides, the presence of P atoms with different valence electrons and electronegativity than S atoms in ZIS could induce the redistribution of electrons within the coordination, thus inducing the charge density to be distributed around the neighboring S atoms. This leads to a decrease in H adsorption–desorption barrier and ΔG_{H^*} being closer to the thermoneutral states. As a result, the inert S2 atoms in ZIS have been activated into potential HER active sites *via* substitutional P filling. Consequently, the optimal P-doped ZIS sample (ZIS-P200) exhibited visible light-driven H_2 evolution from pure water (1.68 μmol h^{-1}) and 0.5 M NaCl as simulated seawater (1.54 μmol h^{-1}) without any sacrificial reagent. On the polar opposite, no activity was observed for the undoped ZIS sample. Apart from that, the application of ZIS-P200 can be implemented into sacrificial agent-free photocatalytic HERs using artificial seawater. As a whole, this work highlights the ingenious kinetic-oriented design of ternary metal chalcogenides *via* heteroatom doping in regulating the atomic-level H adsorption strength and paves a pathway to drive direct photocatalytic seawater splitting under visible light irradiation and ambient conditions.

Conflicts of interest

There are no conflicts to declare.

Acknowledgements

This work was funded by the Ministry of Higher Education (MOHE) Malaysia under Fundamental Research Grant Scheme (FRGS) (Ref. no. FRGS/1/2019/TK02/MUSM/01/1) and Monash University Malaysia under MUM-ASEAN Research Grant Scheme (Ref. no. ASE-000010). B.-J. Ng would like to thank the School of Engineering, Monash University Malaysia for providing the research fellowship under the Engineering Research Accelerator Program.

Notes and references

1 L. K. Putri, B.-J. Ng, W.-J. Ong, H. W. Lee, W. S. Chang and S.-P. Chai, *J. Mater. Chem. A*, 2018, **6**, 3181–3194.
2 Q. Wang and K. Domen, *Chem. Rev.*, 2020, **120**, 919–985.
3 S. Cao, J. Low, J. Yu and M. Jaroniec, *Adv. Mater.*, 2015, **27**, 2150–2176.
4 B.-J. Ng, L. K. Putri, X. Y. Kong, Y. W. Teh, P. Pasbakhsh and S.-P. Chai, *Adv. Sci.*, 2020, **7**, 1903171.
5 B.-J. Ng, L. K. Putri, X. Y. Kong, P. Pasbakhsh and S.-P. Chai, *Chem. Eng. J.*, 2021, **404**, 127030.
6 S. Chen, T. Takata and K. Domen, *Nat. Rev. Mater.*, 2017, **2**, 17050.
7 Y.-H. Chew, B.-J. Ng, J.-Y. Tang, L.-L. Tan and S.-P. Chai, *Sol. RRL*, 2021, **5**, 2100016.
8 X. Guan, F. A. Chowdhury, N. Pant, L. Guo, L. Vayssieres and Z. Mi, *J. Phys. Chem. C*, 2018, **122**, 13797–13802.
9 B. Mishra, S. Mishra, B. Satpati and Y. S. Chaudhary, *ChemSusChem*, 2019, **12**, 3383–3389.
10 S. M. Ji, H. Jun, J. S. Jang, H. C. Son, P. H. Borse and J. S. Lee, *J. Photochem. Photobiol., A*, 2007, **189**, 141–144.
11 F. Sun, J. Qin, Z. Wang, M. Yu, X. Wu, X. Sun and J. Qiu, *Nat. Commun.*, 2021, **12**, 4182.
12 Z. Li, J. Hou, B. Zhang, S. Cao, Y. Wu, Z. Gao, X. Nie and L. Sun, *Nano Energy*, 2019, **59**, 537–544.
13 W. Chen, T. Y. Liu, T. Huang, X. H. Liu and X. J. Yang, *Nanoscale*, 2016, **8**, 3711–3719.
14 Y. Qin, H. Li, J. Lu, Y. Feng, F. Meng, C. Ma, Y. Yan and M. Meng, *Appl. Catal., B*, 2020, **277**, 119254.
15 J. Wang, S. Sun, R. Zhou, Y. Li, Z. He, H. Ding, D. Chen and W. Ao, *J. Mater. Sci. Technol.*, 2021, **78**, 1–19.
16 C. Du, Q. Zhang, Z. Lin, B. Yan, C. Xia and G. Yang, *Appl. Catal., B*, 2019, **248**, 193–201.
17 A. Yan, X. Shi, F. Huang, M. Fujitsuka and T. Majima, *Appl. Catal., B*, 2019, **250**, 163–170.
18 Y. W. Teh, C.-M. Fung, M. K. T. Chee, J. Low, S.-T. Yong and S.-P. Chai, *Mater. Today*, 2021, **43**, 198–212.
19 X. Shi, L. Mao, P. Yang, H. Zheng, M. Fujitsuka, J. Zhang and T. Majima, *Appl. Catal., B*, 2020, **265**, 118616.
20 B.-J. Ng, L. K. Putri, X. Y. Kong, K. P. Y. Shak, P. Pasbakhsh, S.-P. Chai and A. R. Mohamed, *Appl. Catal., B*, 2018, **224**, 360–367.
21 X. Shi, L. Mao, C. Dai, P. Yang, J. Zhang, F. Dong, L. Zheng, M. Fujitsuka and H. Zheng, *J. Mater. Chem. A*, 2020, **8**, 13376–13384.
22 J.-C. Wu, J. Zheng, P. Wu and R. Xu, *J. Phys. Chem. C*, 2011, **115**, 5675–5682.
23 H. Huang, B. Dai, W. Wang, C. Lu, J. Kou, Y. Ni, L. Wang and Z. Xu, *Nano Lett.*, 2017, **17**, 3803–3808.
24 L. Meng, D. Rao, W. Tian, F. Cao, X. Yan and L. Li, *Angew. Chem., Int. Ed.*, 2018, **57**, 16882–16887.
25 Y. Shi, Y. Zhou, D.-R. Yang, W.-X. Xu, C. Wang, F.-B. Wang, J.-J. Xu, X.-H. Xia and H.-Y. Chen, *J. Am. Chem. Soc.*, 2017, **139**, 15479–15485.
26 J. Zhu, L. Hu, P. Zhao, L. Y. S. Lee and K.-Y. Wong, *Chem. Rev.*, 2020, **120**, 851–918.

27 W. Xu, G. Fan, S. Zhu, Y. Liang, Z. Cui, Z. Li, H. Jiang, S. Wu and F. Cheng, *Adv. Funct. Mater.*, 2021, **31**, 2107333.
28 P. Wang, Z. Shen, Y. Xia, H. Wang, L. Zheng, W. Xi and S. Zhan, *Adv. Funct. Mater.*, 2019, **29**, 1807013.
29 H. Huang, X. Feng, C. Du and W. Song, *Chem. Commun.*, 2015, **51**, 7903–7906.
30 K. Yang, Y. Dai and B. Huang, *J. Phys. Chem. C*, 2007, **111**, 18985–18994.
31 J. P. Perdew and M. Ernzerhof, *J. Chem. Phys.*, 1996, **105**, 9982.
32 G. Kresse and D. Joubert, *Phys. Rev. B: Condens. Matter Mater. Phys.*, 1999, **59**, 1758.
33 J. Heyd, G. E. Scuseria and M. Ernzerhof, *J. Chem. Phys.*, 2003, **118**, 8207–8215.
34 S. Zhang, X. Liu, C. Liu, S. Luo, L. Wang, T. Cai, Y. Zeng, J. Yuan, W. Dong, Y. Pei and Y. Liu, *ACS Nano*, 2018, **12**, 751–758.
35 X. Wang, X. Wang, J. Huang, S. Li, A. Meng and Z. Li, *Nat. Commun.*, 2021, **12**, 4112.
36 K. Zhang, J. K. Kim, B. Park, S. Qian, B. Jin, X. Sheng, H. Zeng, H. Shin, S. H. Oh, C.-L. Lee and J. H. Park, *Nano Lett.*, 2017, **17**, 6676–6683.
37 L. K. Putri, B.-J. Ng, C.-C. Er, W.-J. Ong, W. S. Chang, A. R. Mohamed and S.-P. Chai, *Appl. Surf. Sci.*, 2020, **504**, 144427.
38 X. Li, J. Yu, J. Low, Y. Fang, J. Xiao and X. Chen, *J. Mater. Chem. A*, 2015, **3**, 2485–2534.
39 Y.-H. Chew, B.-J. Ng, X. Y. Kong, L. K. Putri, J.-Y. Tang, L.-L. Tan and S.-P. Chai, *Sustainable Energy Fuels*, 2020, **4**, 1822–1827.
40 K.-i. Okazaki, Y. Nakato and K. Murakoshi, *Phys. Rev. B: Condens. Matter Mater. Phys.*, 2003, **68**, 035434.
41 L. Lin, Y. Ma, J. Wu, F. Pang, J. Ge, S. Sui, Y. Yao, R. Qi, Y. Cheng, C.-g. Duan, J. Chu and R. Huang, *J. Phys. Chem. C*, 2019, **123**, 20949–20959.
42 Y. Zhang, O. Pluchery, L. Caillard, A.-F. l. Lamic-Humblot, S. Casale, Y. J. Chabal and M. Salmeron, *Nano Lett.*, 2015, **15**, 51–55.
43 L. K. Putri, B.-J. Ng, K. H. Tan, F. S. Lim, W.-J. Ong, W. S. Chang and S.-P. Chai, *Catal. Today*, 2018, **315**, 93–102.
44 C.-Y. Su, L.-C. Wang, W.-S. Liu, C.-C. Wang and T.-P. Perng, *ACS Appl. Mater. Interfaces*, 2018, **10**, 33287–33295.
45 W. Zhang, Y. Fu, Q. Peng, Q. Yao, X. Wang, A. Yu and Z. Chen, *Chem. Eng. J.*, 2020, **394**, 124822.
46 R. Shi, H.-F. Ye, F. Liang, Z. Wang, K. Li, Y. Weng, Z. Lin, W.-F. Fu, C.-M. Che and Y. Chen, *Adv. Mater.*, 2018, **30**, 1705941.
47 J. Wang, X. Li, B. Wei, R. Sun, W. Yu, H. Y. Hoh, H. Xu, J. Li, X. Ge, Z. Chen, C. Su and Z. Wang, *Adv. Funct. Mater.*, 2020, **30**, 1908708.
48 C. Du, B. Yan, Z. Lin and G. Yang, *J. Mater. Chem. A*, 2020, **8**, 207–217.
49 T. F. Jaramillo, K. P. Jørgensen, J. Bonde, J. H. Nielsen, S. Horch and I. Chorkendorff, *Science*, 2007, **317**, 100.
50 Z. Luo, Y. Ouyang, H. Zhang, M. Xiao, J. Ge, Z. Jiang, J. Wang, D. Tang, X. Cao, C. Liu and W. Xing, *Nat. Commun.*, 2018, **9**, 2120.
51 R. Ye, P. del Angel-Vicente, Y. Liu, M. J. Arellano-Jimenez, Z. Peng, T. Wang, Y. Li, B. I. Yakobson, S.-H. Wei, M. J. Yacaman and J. M. Tour, *Adv. Mater.*, 2016, **28**, 1427–1432.
52 T. Song, P. Zhang, T. Wang, A. Ali and H. Zeng, *Nanoscale*, 2018, **10**, 2275–2284.
53 J. Zhang, W. Hu, S. Cao and L. Piao, *Nano Res.*, 2020, **13**, 2313–2322.
54 W.-J. Ong, J.-J. Yeong, L.-L. Tan, B. T. Goh, S.-T. Yong and S.-P. Chai, *RSC Adv.*, 2014, **4**, 59676–59685.
55 B.-J. Ng, L. K. Putri, X. Y. Kong, P. Pasbakhsh and S.-P. Chai, *Appl. Catal., B*, 2020, **262**, 118309.
56 Y. Zhong, Y. Wu, B. Chang, Z. Ai, K. Zhang, Y. Shao, L. Zhang and X. Hao, *J. Mater. Chem. A*, 2019, **7**, 14638–14645.
57 G. Cui, W. Wang, M. Ma, J. Xie, X. Shi, N. Deng, J. Xin and B. Tang, *Nano Lett.*, 2015, **15**, 7199–7203.
58 A. J. Simamora, T. L. Hsiung, F. C. Chang, T. C. Yang, C. Y. Liao and H. P. Wang, *Int. J. Hydrogen Energy*, 2012, **37**, 13855–13858.
59 S. Liu, Y. Ma, D. Chi, Y. Sun, Q. Chen, J. Zhang, Z. He, L. He, K. Zhang and B. Liu, *Int. J. Hydrogen Energy*, 2022, **47**, 9220–9229.
60 X. Y. Kong, W. L. Tan, B.-J. Ng, S.-P. Chai and A. R. Mohamed, *Nano Res.*, 2017, **10**, 1720–1731.
61 B.-J. Ng, L. K. Putri, L.-L. Tan, P. Pasbakhsh and S.-P. Chai, *Chem. Eng. J.*, 2017, **316**, 41–49.
62 J. Qin, Q. Zhao, Y. Zhao, Y. Wu, B. Pan and C. Wang, *J. Phys. Chem. C*, 2021, **125**, 23813–23820.
63 X. Y. Kong, B.-J. Ng, K. H. Tan, X. Chen, H. Wang, A. R. Mohamed and S.-P. Chai, *Catal. Today*, 2018, **314**, 20–27.
64 L. K. Putri, B. J. Ng, W.-J. Ong, H. W. Lee, W. S. Chang and S.-P. Chai, *ACS Appl. Mater. Interfaces*, 2017, **9**, 4558–4569.
65 J.-Y. Tang, X. Y. Kong, B.-J. Ng, Y.-H. Chew, A. R. Mohamed and S.-P. Chai, *Catal. Sci. Technol.*, 2019, **9**, 2335–2343.

